International Journal of Fatigue 172 (2023) 107586



Contents lists available at ScienceDirect

International Journal of Fatigue

journal homepage: www.elsevier.com/locate/ijfatigue





Short crack propagation near coherent twin boundaries in nickel-based superalloy

Xiaoxian Zhang *, Fionn P.E. Dunne

Department of Materials, Imperial College London, SW7 2AZ, UK

A B S T R A C T

Short crack propagation near a coherent twin boundary in polycrystal nickel alloy is investigated with 3D crystal plasticity extended finite element modelling (CP-XFEM), utilising reconstructed experimentally characterised microstructures and crack path observations. Short 3D cracks at coherent twin boundaries are shown to grow on parallel (1 1 1) slip planes at very high rate so as to be an intrinsic part of the nucleation process. This is found to occur predominantly because of the stress states established by twin/parent constraint driven by the local elastic anisotropy. If elastic isotropy is modelled, crack growth is found to be non-planar and inclined to the twin boundary. The twin/parent twist angle is also found to influence local stress state, such that the actual 60° twist angle gives rise to the highest local stresses, preferential crack nucleation and rapid growth parallel to the twin boundary, and the deviations from 60° change the crack morphology and rate of growth.

1. Introduction

Short crack propagation is a key aspect of fatigue fracture in ductile metals and is microstructure-sensitive and associated with grain crystallography and morphology, as commonly observed in experiments [1]. These short cracks propagate from their nucleation points in tortuous paths and with varying rates, which cannot be quantified by linear elastic fracture mechanics as for long cracks [2]. As the key stage after fatigue crack nucleation (roughly covering ~ 80% lifetime) [3], understanding the mechanism of these paths and rates is significant for improved design of reliable engineering components.

Polycrystal nickel alloys are commonly used in aero-engine discs due to their excellent fatigue and creep resistance [4]. However, these alloys have an unavoidable microstructure of annealing twin boundaries if manufactured by powder metallurgy [5]. Annealing twin boundaries are well known as the preferential fatigue crack nucleation sites in polycrystal nickel alloys such as René 88DT [6], RR1000 [7] and IN100 [8]. Interestingly, the associated short crack propagations have been found to be strongly dependent upon the nature of adjacent twin boundaries (TB) [6,8-10]. In respect of crack path, two typical cases can be identified, namely the crack path is parallel to the TB [10-12], or it is inclined to the TB [13,14]. Parallel cracks are always found to occur in large grains containing TBs with high Schmid factor [10]. With respect to the sample surface, a parallel crack path is aligned with the TB and deflected at the end of TB as the microstructure changes ahead of the crack-tip [15]. In relation to the sub-surface, the fracture plane is dominated by one of the {1 1 1} slip planes and is parallel to the TB [16]. It is anticipated that parallel cracks relate to a high crack propagation rate because they preferentially grow along the favoured slip plane within which dislocations glide parallel to the TB without resistance from either constraint or grain boundary effects [17]. As a consequence, cracks parallel to and near TBs are detrimental to fatigue life, and as such it is important to understand the role of the local microstructural features in facilitating this in order to design better alloys. The inclined cracks may be nucleated along a persistent slip band (PSB) which is inclined to TB, and this initiation process are driven by a stress concentration near the TB which is caused by the PSB impingement to TB [13]. In addition, TB can be a type of barrier to resist the short crack propagation due to the high twist angle [13,18]. This strengthening behaviour for fatigue lifetime is experimentally observed in stainless steel, in which a high fraction of Σ3 grain boundaries (twin boundary in FCC) clearly shows a low crack propagation rate [18]. However, this type of crack is often observed to nucleate at a location which is well-removed from the TB, which is quite different to the cases of parallel and inclined cracks nucleated near the TB. The advantages and disadvantages (strengthening versus crack nucleation) of twin boundaries (Σ3 in FCC) lead to scattered results [19] but TBs remain an important factor controlling fatigue failure.

Short crack propagation depends on the local stress state ahead of the crack-tip [20,21]. In polycrystal alloys, the stress fields are heterogeneous due to crystal constraint effects resulting from elastic anisotropy in which the elastic responses (eg. Young's modulus along loading direction) of the two adjacent grains are different, leading to an incompatibility stress near the twin boundaries [22]. Additional strong

* Corresponding author.
E-mail address: xiaoxian.zhang18@imperial.ac.uk (X. Zhang).

https://doi.org/10.1016/j.ijfatigue.2023.107586
Received 19 December 2022; Received in revised form 12 February 2023; Accepted 17 February 2023
Available online 18 February 2023
0142-1123/© 2023 The Authors. Published by Elsevier Ltd. This is an open access article under the CC BY-NC-ND license (http://creativecommons.org/licenses/by-nc-nd/4.0/).

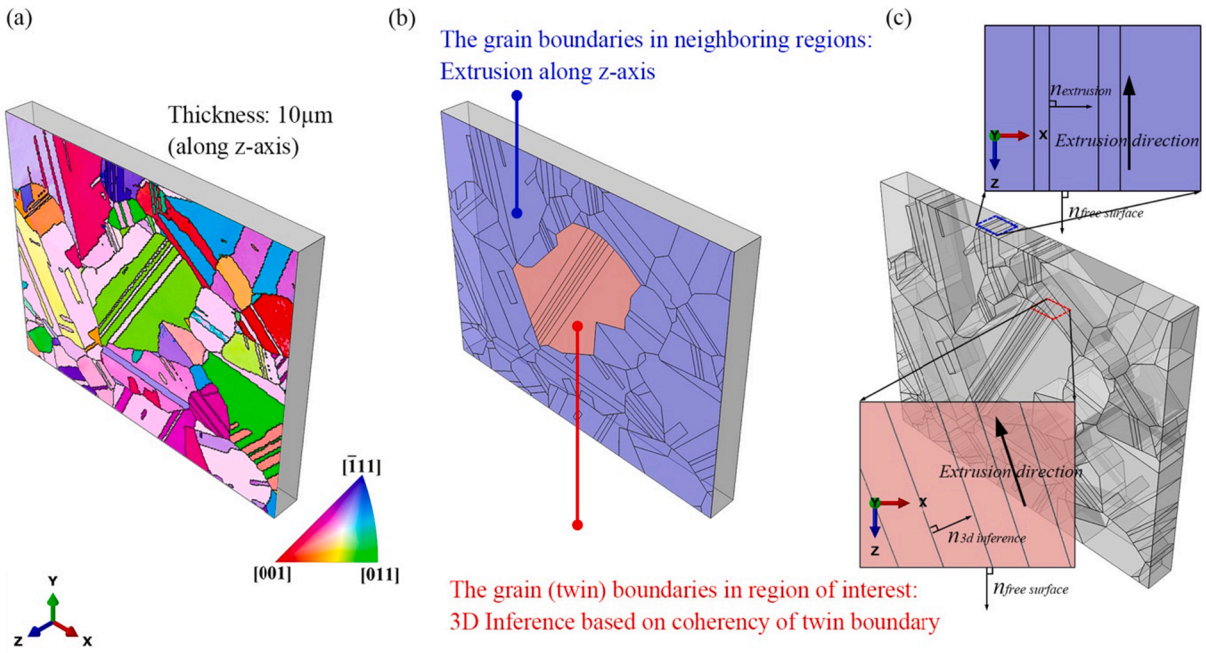

Fig. 1. (a) EBSD map [22]; (b) Inference of sub-surface microstructure based on coherent twin boundary in FCC. Blue region refers to an extrusion assumption along the free surface normal; red region refers to a grain boundary aligned with the stacking fault plane of twins (one of {1 1 1} slip planes with common ⟨1 1 1⟩ twist axis); (c) Two sub-views projected to XZ plane, illustrating the geometric difference (extrusion directions) between extrusion and coherent TB regions. (For interpretation of the references to colour in this figure legend, the reader is referred to the web version of this article.)

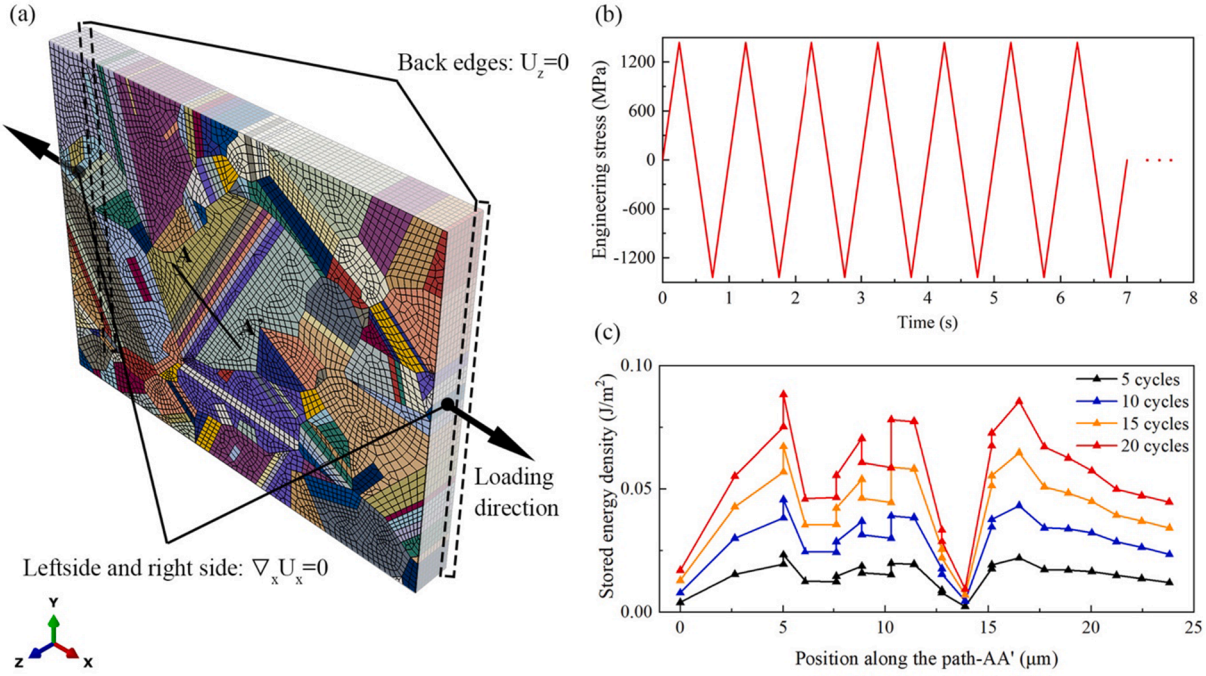

Fig. 2. (a) Loading boundary conditions, the cyclic stress along global-x axis is applied on the left and right sides which remain planar during loading; (b) Stress-control of loading history. (c) Accumulation of stored energy density along the path-AA'.

Table 1
Material properties for polycrystal nickel alloy (René 88DT).

C_{11}(GPa)	C_{12}(GPa)	C_{44}(GPa)	τ_0(MPa)	b(μm)
273.6	170.7	125.8	420	2.54x10^{-4}
λ(μm^{-2})	ν(s^{-1})	ΔF(J/atom)	ρ^{m}_{SSD}(μm^{-2})	ΔV(μm^3)
12	1.0x10^{11}	8.2x10^{-20}	0.02	22 b^3

stress concentrations local to TBs have been reported as a result of the impinging of persistent slip bands which are inclined to the TB [13,14]. In addition, individual slip localizations near TBs have been observed by HR-DIC and Heaviside-DIC, which have been demonstrated as a precursor to parallel crack initiation including, nucleation and short crack propagation [11,17]. These localizations are strongly sensitive to the neighbouring crystallography and a change to the local stress/strain fields ahead of crack-tip can be expected to occur as it propagates near to

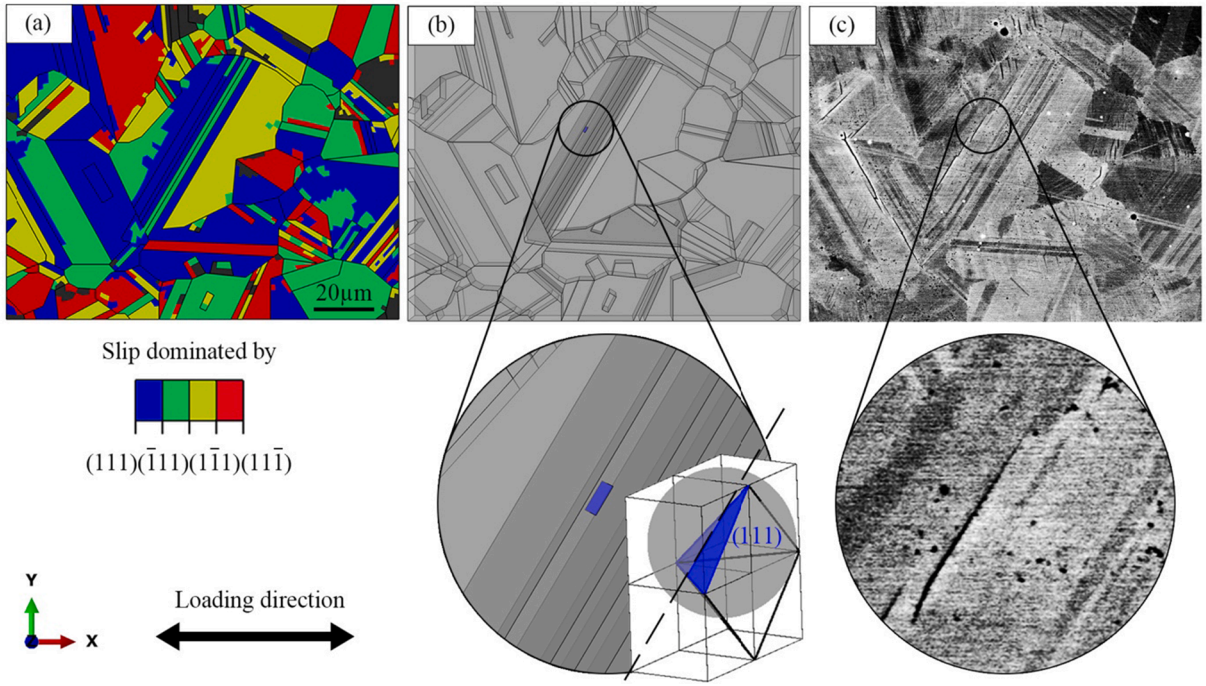

Fig. 3. (a) Slip activation after 3 cycles where colour is used to differentiate the four slip plane types, no pre-crack is inserted at this stage; (b) The pre-crack aligned with twin boundary and (1 1 1) plane of the corresponding grain; (c) SEM figure in the same region, which is taken at the end of failure [22];

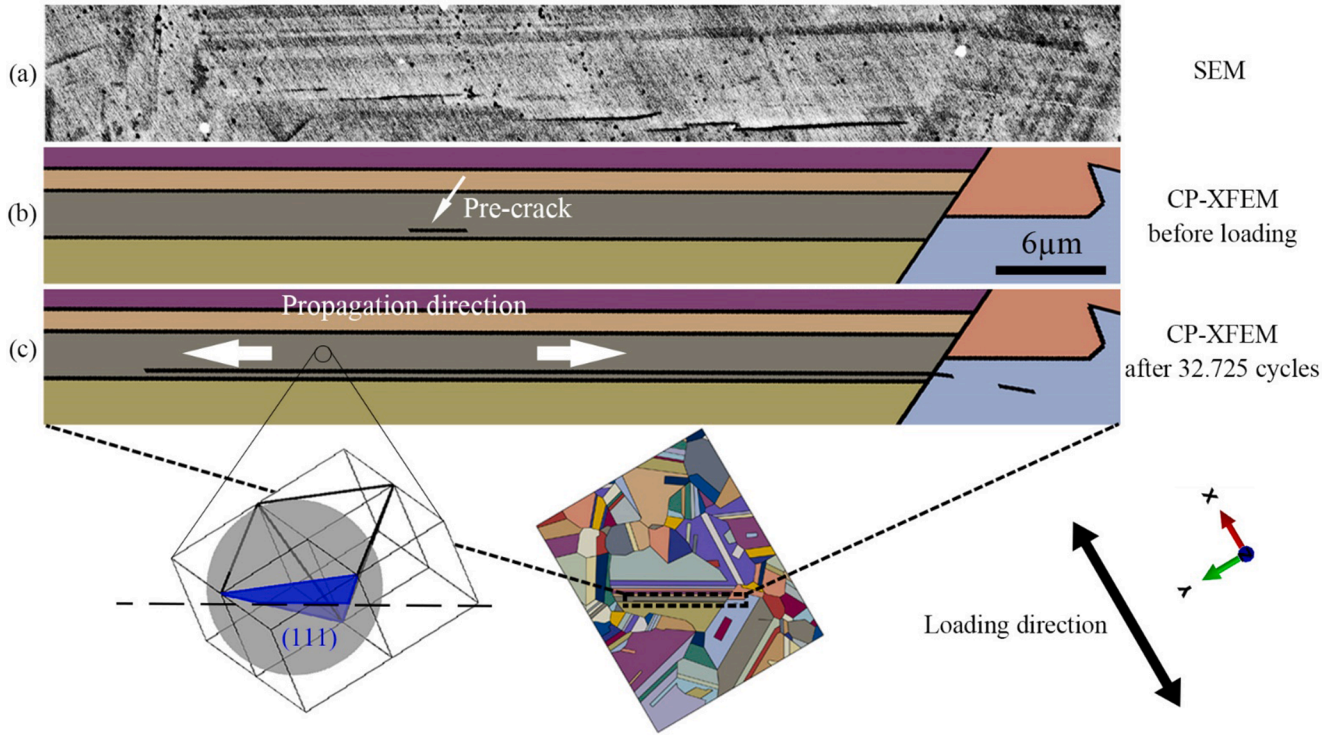

Fig. 4. (a) SEM figure captured at the end of failure time [22]; (b) Crack path obtained from CP-XFEM reflecting the same region as Fig. 4(a) and shown just prior to loading. (c) Crack paths obtained after ~ 33 cycles with CSED = 0.10 J/m^2. Also inset are the full modelled microstructure within which the twinned region is marked, and the twin plane orientation.

a TB [22]. The loading directions with respect to TB (in bi-crystal configuration) have been demonstrated to be a key factor in affecting the dislocation arrangement and crack morphologies [23,24]. In addition, the elastic anisotropy is found to be key to nickel crack initiation near TBs, which can result in stronger strain localization aligned with TBs [22,25]. Hence, understanding the mechanistic link between the microstructures and the micromechanics (stress concentration, strain localization, slip activation, etc) ahead of the crack-tip is important, particularly in the context of structural integrity of these alloys which contain TBs.

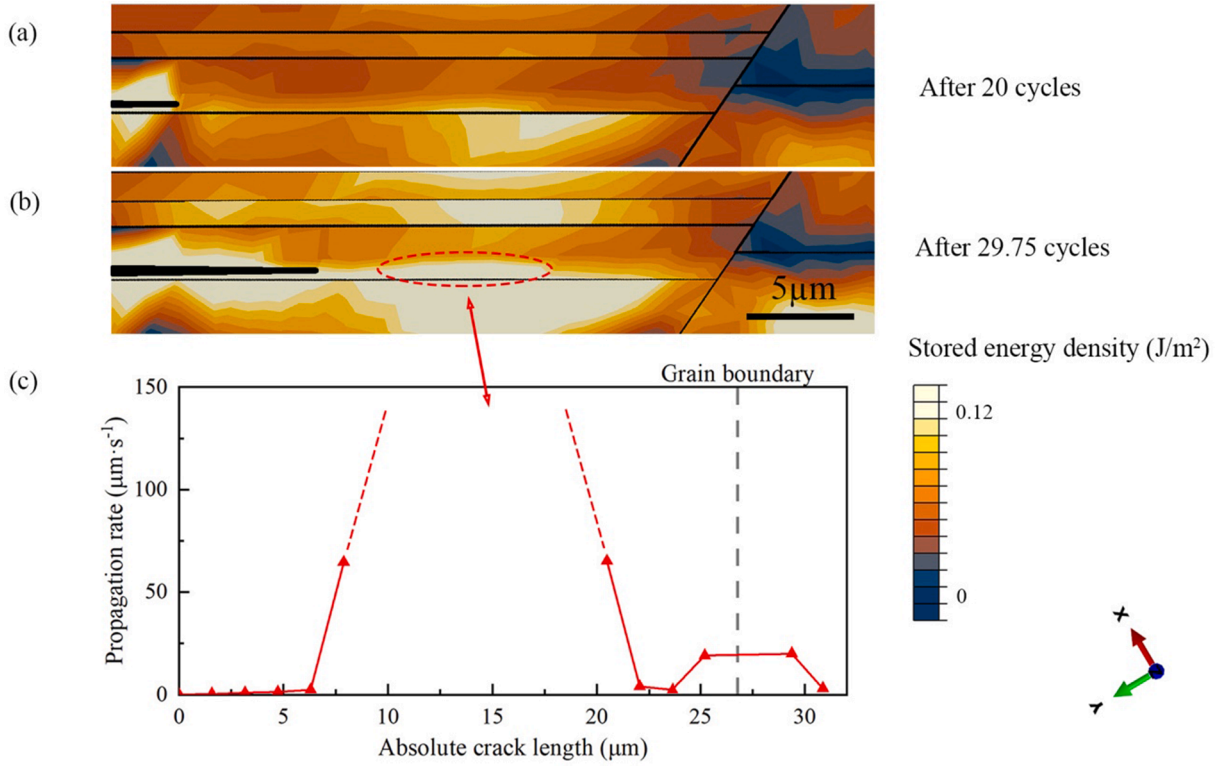

Fig. 5. Stored energy density field ahead of crack-tip after (a) 20 cycles, (b) 29.75 cycles. (c) Crack propagation rate calculated from the path on free surface. The (a), (b) and (c) are positioned with each other along the absolute crack length (horizontal axis in (c)).

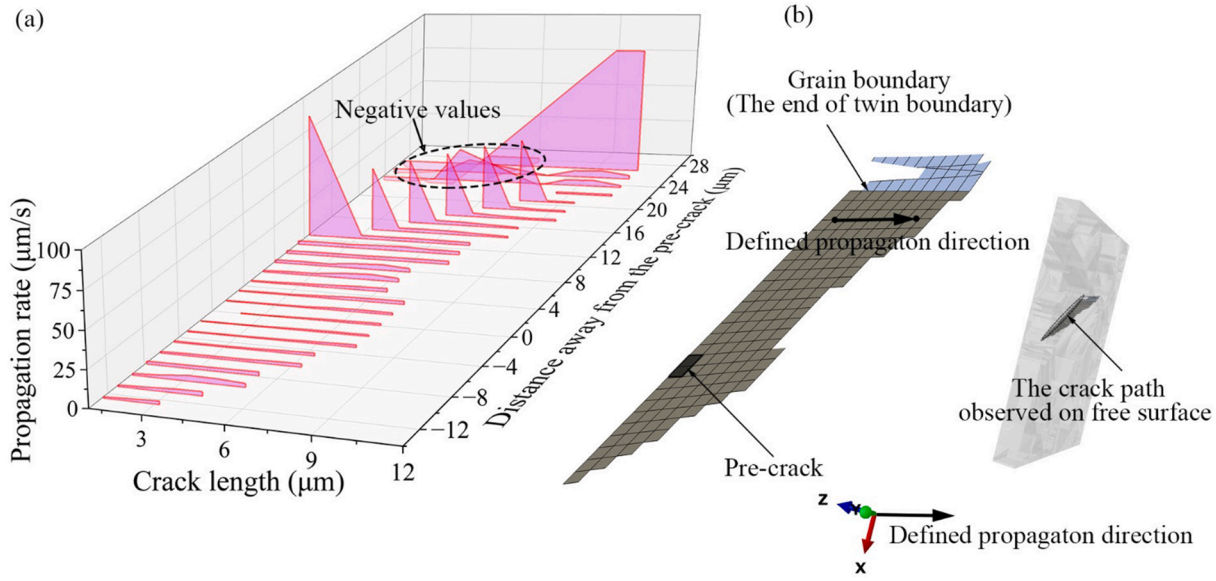

Fig. 6. (a) Decomposed crack propagation rate of crack plane in 2D form, the crack length is measured from the free surface along the direction defined in Fig. 6(b), the distance away from the pre-crack is measured from the pre-crack (shown in black in Fig. 6(b)) along the free-surface crack path. (b) A specified view of the fracture plane after 32.5 cycles, two grains are differentiated by two differing colours, the location of this fracture plane is shown in the right-side within the full finite element model.

In this study, systematic investigations are presented to assess the effect of crystallography in crack propagation near a TB, employing 3D CP-XFEM modelling developed from EBSD scanning and fatigue experiments. The CP-XFEM modelling replicates the experimental loading and boundary conditions, and employs the elastic stored energy density as the fatigue criterion, which is supported based on a crystal plasticity approximation to the dislocation configurational energy density [26,27]. Good validity of this criterion has been demonstrated by a series of integrated experimental and modelling studies for FCC, BCC and HCP crystal structures at micron-scale [28-30]. In this study, anisotropic elasticity is employed to consider the stress concentration near TBs [10], and crystal plasticity modelling is employed to consider the slip/plastic strain localization near TBs [10,22]. 3D crack paths and growth rates at twin boundaries are analysed, in particular addressing the conditions

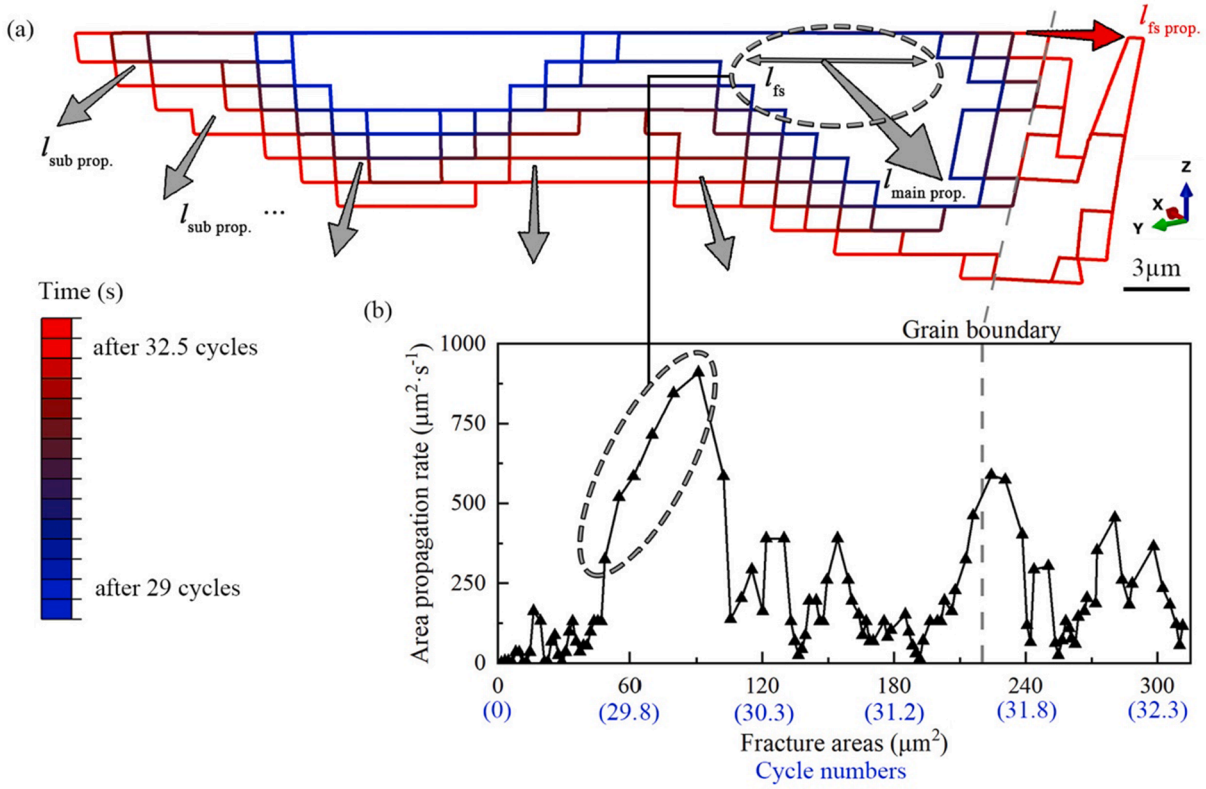

Fig. 7. (a) Crack front profile (frame of fracture plane) at differing cycles with same increments. The view direction is normal to the parallel fracture plane. (b) The area propagation rate which is calculated from the fractured area per time increment. The location of the grain boundary (the end of TB) corresponding to the fracture area achieved when the crack front first interacts with the GB is marked by grey dashed lines.

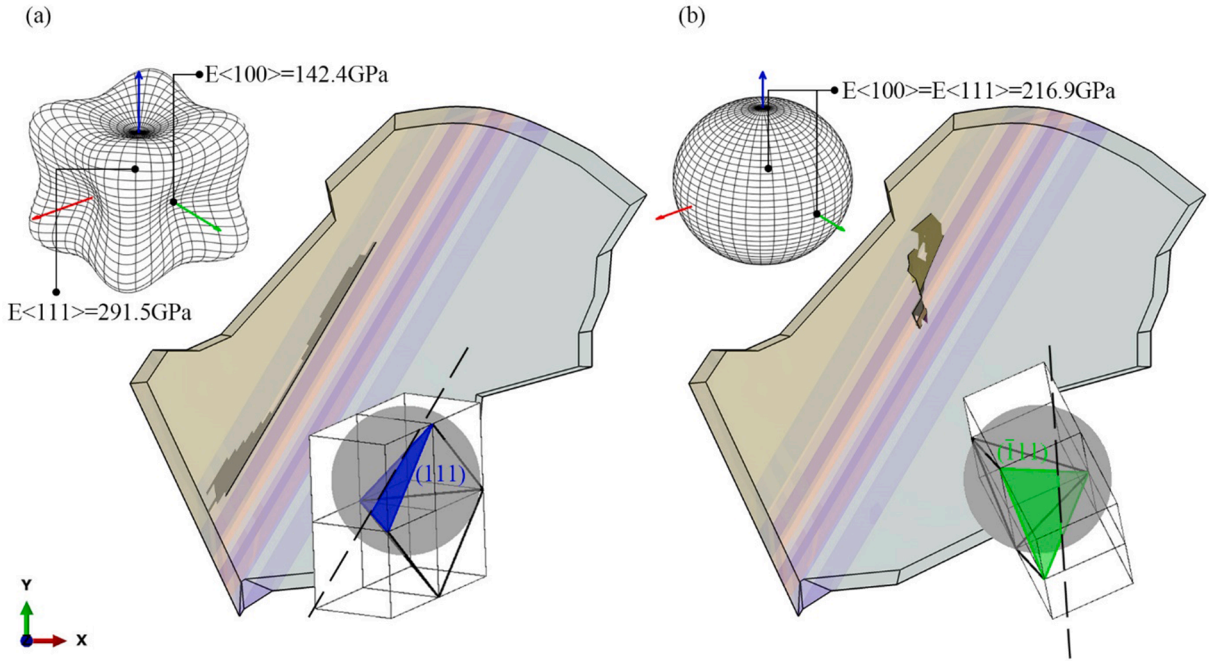

Fig. 8. (a) Predicted 3D crack morphology assuming 'natural' elastic anisotropy, for cycle 30; (b) predicted 3D crack morphology assuming elastic isotropy, for cycle 23.

ling to crack growth parallel to twin boundaries. The role of TB constraint from local elastic anisotropy is investigated, and followed by a study of the twin-parent twist angle on both crack morphology and growth direction.

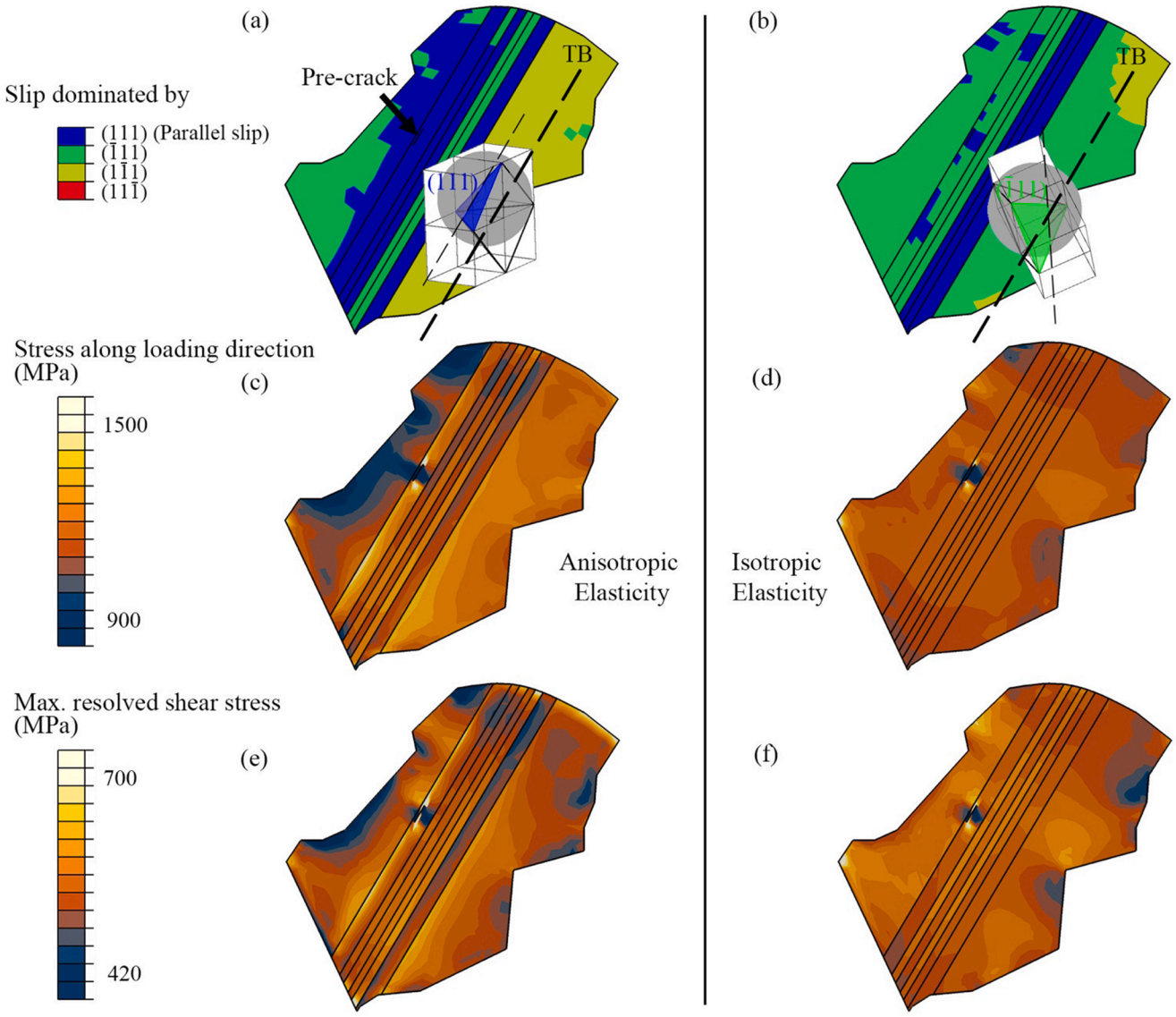

Fig. 9. Slip activation ((a) and (b)), loading direction stress ((c) and(d)), and maximum resolved shear stress ((e) and (f)) for anisotropic elasticity (left) and isotropic elasticity (right) at the peak loading of the 2nd cycle.

2. Methodology

2.1. Crystal plasticity and XFEM

A dislocation-based crystal plasticity model is adopted here to investigate the microstructurally sensitive short crack propagation in polycrystal nickel-based alloy. The plastic velocity gradient $\boldsymbol{L}^p$ is determined in terms of slip system directions and normals by [31]

$$\boldsymbol{L}^p = \sum_{i=1}^{12} \dot{\gamma}^i \boldsymbol{s}^i \otimes \boldsymbol{n}^i \tag{1}$$

where $\boldsymbol{s}^i$ and $\boldsymbol{n}^i$ are the slip direction and plane normal of the ith slip system respectively; the reference configurations of slip systems $\{1\,1\,1\}\langle 1\,1\,0\rangle$ are shown in Apendix. 1. $\dot{\gamma}^i$ is slip rate, which considers both thermal activated dislocation escape and glide, and athermal slip system hardening processes as a result of both sessile statistically stored (SSD) and geometrically necessary (GND) dislocations [32,33]. The slip rule is given by

$$\dot{\gamma}^i = \rho_{SSD}^m b^2 \nu \exp\left(-\frac{\Delta F}{kT}\right) \sinh\left(\frac{\left|\tau^i - \tau_C^i\right| \Delta V}{kT}\right) \tag{2}$$

where ρ_{SSD}^m is the density of mobile dislocations, b the magnitude of Burgers vector, ν the attempt frequency of dislocations in jumping the energy barrier, ΔF the activation energy associated with dislocation escape and ΔV is the activation volume. k is the Boltzmann constant and T the environment temperature. τ^i is the resolved shear stress on the ith slip system, and τ_C^i is the corresponding slip system strength, which couples with accumulation of slip following dislocation hardening given by

$$\tau_C = \tau_0 + \alpha G b \sqrt{\rho_{SSD}^s + \rho_{GND}} \tag{3}$$

where τ_0 is the initial intrinsic slip strength, α the coefficient of Taylor hardening, G the shear modulus, ρ_{SSD}^s and ρ_{GND} are the densities of SSDs and GNDs respectively. ρ_{SSD}^s is assumed to be evolving according to an isotropic strain hardening law

$$\dot{\rho}_{SSD}^s = \lambda \dot{p} \tag{4}$$

where λ is a hardening coefficient, and $\dot{p}$ is the rate of effective plastic

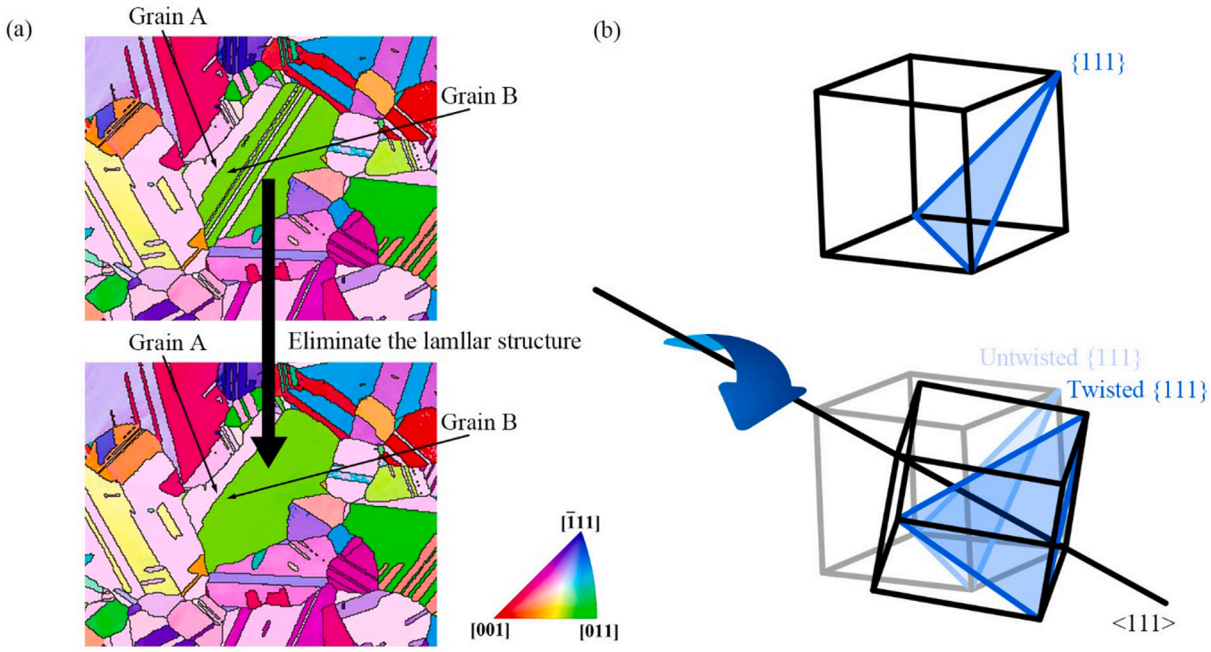

Fig. 10. (a) Microstructure modification to eliminate the effect of lamellar structure; (b) schematic diagram of the TB twist implemented in the model.

strain, which is defined as

$$\dot{p} = \left(\frac{2}{3}\dot{\boldsymbol{\varepsilon}}^{\mathrm{p}} : \dot{\boldsymbol{\varepsilon}}^{\mathrm{p}}\right)^{\frac{1}{2}} = \left[\frac{2}{3}\left(\left(\dot{\varepsilon}^{p}_{xx}\right)^{2} + \left(\dot{\varepsilon}^{p}_{yy}\right)^{2} + \left(\dot{\varepsilon}^{p}_{zz}\right)^{2} + 2\left(\dot{\varepsilon}^{p}_{xy}\right)^{2} + 2\left(\dot{\varepsilon}^{p}_{yz}\right)^{2} + 2\left(\dot{\varepsilon}^{p}_{xz}\right)^{2}\right)\right]^{\frac{1}{2}} \tag{5}$$

where the plastic strain rate $\dot{\boldsymbol{\varepsilon}}^{\boldsymbol{p}}$ is calculated by the decomposition of $\boldsymbol{L}^{\boldsymbol{p}}$, in which the symmetric part is the plastic strain rate

$$\dot{\boldsymbol{\varepsilon}}^{\boldsymbol{p}} = \mathrm{sym}[\boldsymbol{L}^{\boldsymbol{p}}] \tag{6}$$

For most of conventional structural metals includes nickel alloy, only very small amounts of elastic strain can be carried. Hence, the additive rate of deformation decomposition can be employed as

$$\dot{\boldsymbol{\varepsilon}} = \dot{\boldsymbol{\varepsilon}}^{\boldsymbol{e}} + \dot{\boldsymbol{\varepsilon}}^{\boldsymbol{p}} \tag{7}$$

where $\dot{\boldsymbol{\varepsilon}}$ is strain rate and $\dot{\boldsymbol{\varepsilon}}^{\boldsymbol{e}}$ is elastic strain rate. Hence, the Jaumann stress rate (the stress rate that results purely from the constitutive response of the material and not from rigid body rotation [37]) can be calculated by Hooke's law

$$\widehat{\boldsymbol{\sigma}} = \boldsymbol{C} : (\dot{\boldsymbol{\varepsilon}} - \dot{\boldsymbol{\varepsilon}}^{\boldsymbol{p}}) \tag{8}$$

where $\boldsymbol{C}$ is the stiffness tensor. Finally, the Cauchy stress rate (material rate of stress, considered rigid body rotation) is calculated by

$$\dot{\boldsymbol{\sigma}} = \widehat{\boldsymbol{\sigma}} + \boldsymbol{W}\boldsymbol{\sigma} - \boldsymbol{\sigma}\boldsymbol{W} \tag{9}$$

where $\boldsymbol{\sigma}$ is the current stress state, more details about this constitutive law can be found in [32,37].

GND density accommodates the lattice curvature which is calculated from Nye's dislocation tensor $\boldsymbol{\Lambda}$ [34] given by [35]

$$\boldsymbol{\Lambda} = -\left(\nabla \times \left(F^{p}\right)^{T}\right)^{T} = \sum_{i=1}^{12} \rho^{i}_{Gs}\boldsymbol{b}^{i} \otimes \boldsymbol{s}^{i} + \rho^{i}_{Gen}\boldsymbol{b}^{i} \otimes \boldsymbol{n}^{i} + \rho^{i}_{Get}\boldsymbol{b}^{i} \otimes \boldsymbol{t}^{i} \tag{10}$$

where $\boldsymbol{s}^{i}$, $\boldsymbol{n}^{i}$ and $\boldsymbol{t}^{i}$ are the three orthogonal unit vectors in which ρ^{i}_{Gs} is the density of screw dislocations aligns with $\boldsymbol{s}^{i}$, ρ^{i}_{Gen} the density of edge dislocations aligns with $\boldsymbol{n}^{i}$, and ρ^{i}_{Get} is the density of edge dislocation aligns with $\boldsymbol{t}^{i}$. Because there are 12 slip systems in FCC nickel crystals, the GND tensor comprises 36 independent variables (12 edge branches, 12 screw branches parallel to $\boldsymbol{n}^{i}$, 12 edge branches parallel to $\boldsymbol{t}^{i}$), which need to be solved from nine equations. These equations can be re-written in matrix form as

$$\widehat{\boldsymbol{\Lambda}} = \boldsymbol{A}\boldsymbol{\rho}_{\boldsymbol{GND}} \tag{11}$$

where $\widehat{\boldsymbol{\Lambda}}$ is a 9×1 column vector of Nye's dislocation tensor, and $\boldsymbol{A}$ a 9×36 matrix containing the basis tensors $\boldsymbol{b}^{i} \otimes \boldsymbol{s}^{i}, \boldsymbol{b}^{i} \otimes \boldsymbol{n}^{i}, \boldsymbol{b}^{i} \otimes \boldsymbol{t}^{i}$. $\boldsymbol{\rho}_{\boldsymbol{GND}}$ is a 36×1 column vector of GND components. However, the 36 independent GND components may generate a non-uniqueness problem with the above nine equations. Hence here, the L_2 norm of GND density minimization is used to determine the local GND density because it enables a unique solution and it's easier in mathematic processing [36], and an overall density determined by

$$\rho_{GND} = \sqrt{\sum_{i=1}^{12}\left\{\left(\rho^{i}_{Gs}\right)^{2} + \left(\rho^{i}_{Gen}\right)^{2} + \left(\rho^{i}_{Get}\right)^{2}\right\}} \tag{12}$$

In this study, elastic stored energy density is investigated as the primary driving force for short crack growth, which has been utilized in several alloys and shows good agreement with experimental observations [28-30]. The evolution of elastic stored energy density is calculated from

$$G = \int \dot{G} dN \tag{13}$$

where $\dot{G}$ is the elastic stored energy density accumulated per cycle, which can be calculated by

$$\dot{G} = \int \frac{\xi\boldsymbol{\sigma} : \mathrm{d}\boldsymbol{\varepsilon}^{\boldsymbol{p}}}{\sqrt{\rho_{SSD} + \rho_{GND}}} \tag{14}$$

where ξ is the coefficient which specifies the fraction of dissipated energy that is stored in dislocation structure. Here ξ is chosen to be 0.05 [26]. To reduce the mesh-sensitivity's effect, a non-local averaging method is introduced based on [38] to calculate the elastic stored energy density, in which the quantities of integration point are calculated from a weighting sum over the neighbouring integration points within a defined radius, l.

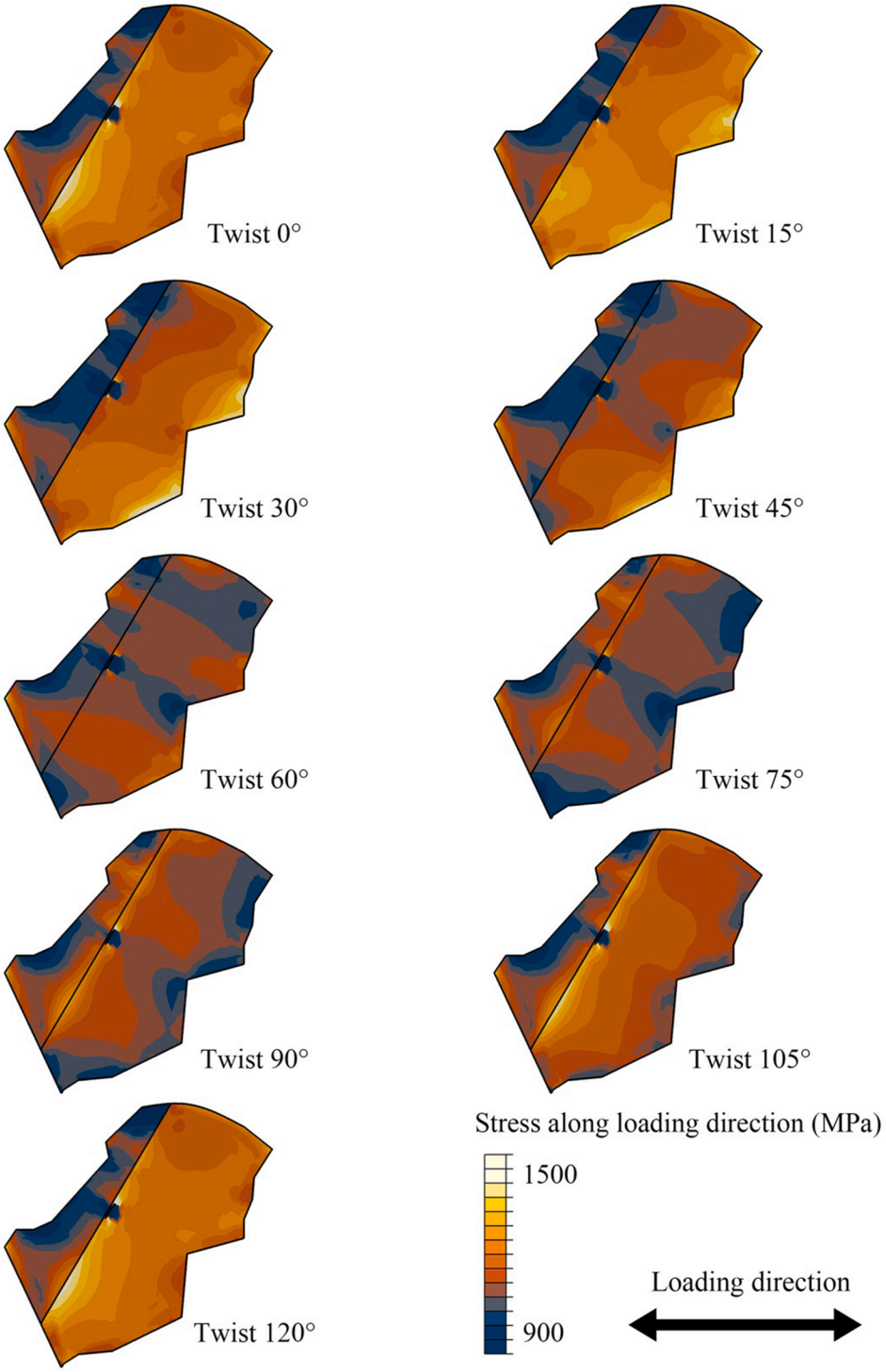

Fig. 11. Loading-direction stress fields near the TB for differing twin/parent twist angles, at the peak of loading in the 2nd cycle.

$$G^{nl} = \sum_{1}^{n}\left[G_i \frac{g(r)}{\sum_1^n g(r)}\right] \tag{15}$$

$$g(r) = e^{-\frac{\pi r^2}{l^2}} \tag{16}$$

where n is the number of neighbouring integration points, G_i is the local elastic stored energy at the integration point i and r is the distance away from the integration point. l is the length scale over which the dislocation structures that is dominated by GND density. In previous simulations, this length has generally been taken to correspond to a suitably small fraction of the key microstructural feature size. Here, 5 μm is arbitrary chosen which equals half of the plate thickness based on previous experiences [39].

XFEM is employed to introduce and propagate fatigue cracks. This method has been implemented in Abaqus with an additional user-defined damage subroutine. XFEM enables the discontinuities modelling such as a growing crack in solid parts, meanwhile alleviating the requirement of remeshing at crack tips. In this method, the element to contain the crack is bisected by introducing phantom nodes when this element's damage criterion achieves to a critical value. The bisection

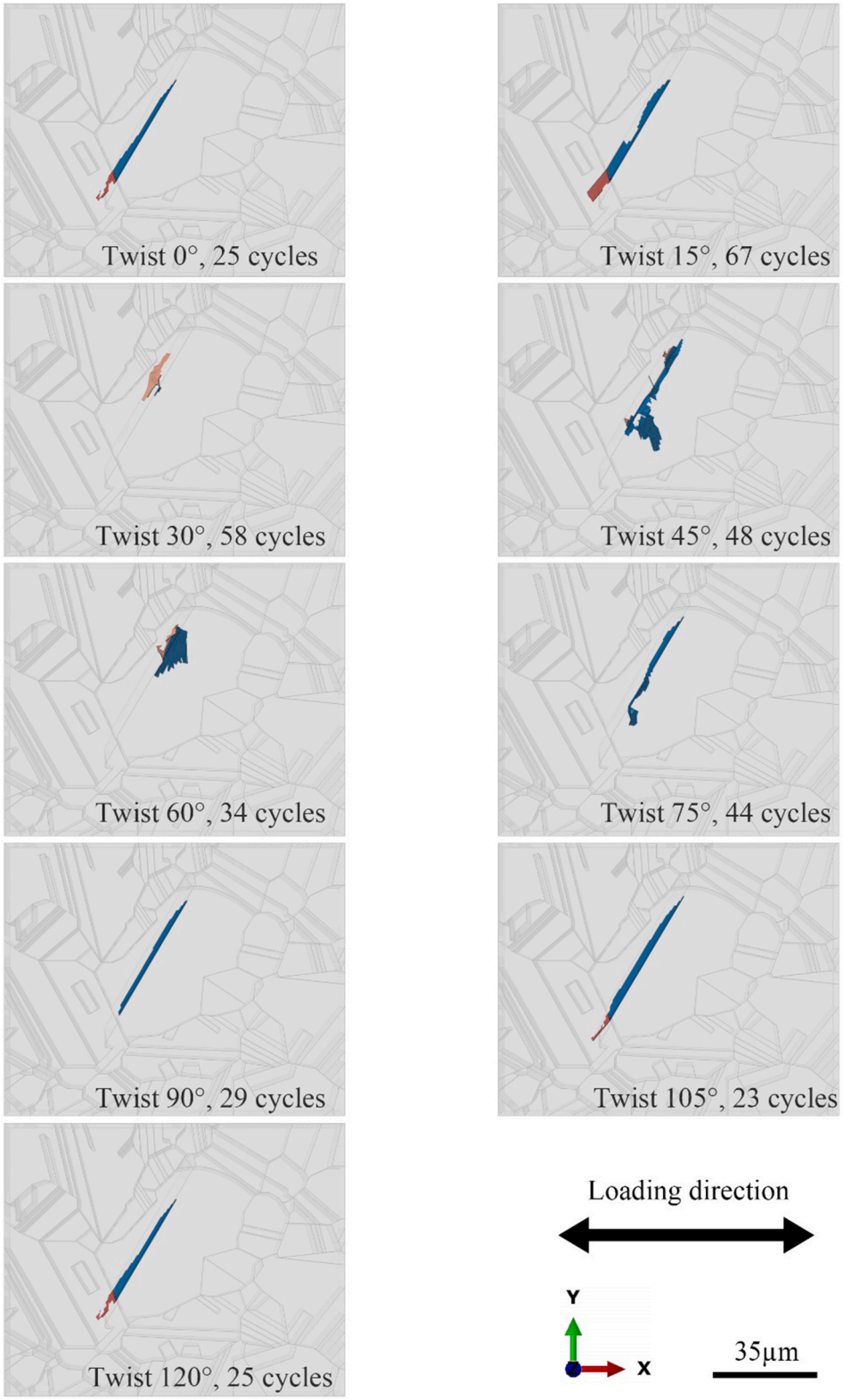

Fig. 12. The fracture planes for the differing TB/GB twist angles shown. (A different number of loading cycles is required to achieve the crack lengths shown in each case.).

plane is the fracture plane, and it can be set through the user defined damage subroutine. In this study, the fracture/bisection plane is set as the slip plane which contains the highest slip accumulation, and the damage criterion chosen for crack advance is the non-local stored energy density (Eq. (15)) once a critical elastic stored energy density value is achieved. The CP-XFEM introduced in this study has been used in previous works with differing crystal materials, more details about convergence and algorithm studies can be found in [21,39-41].

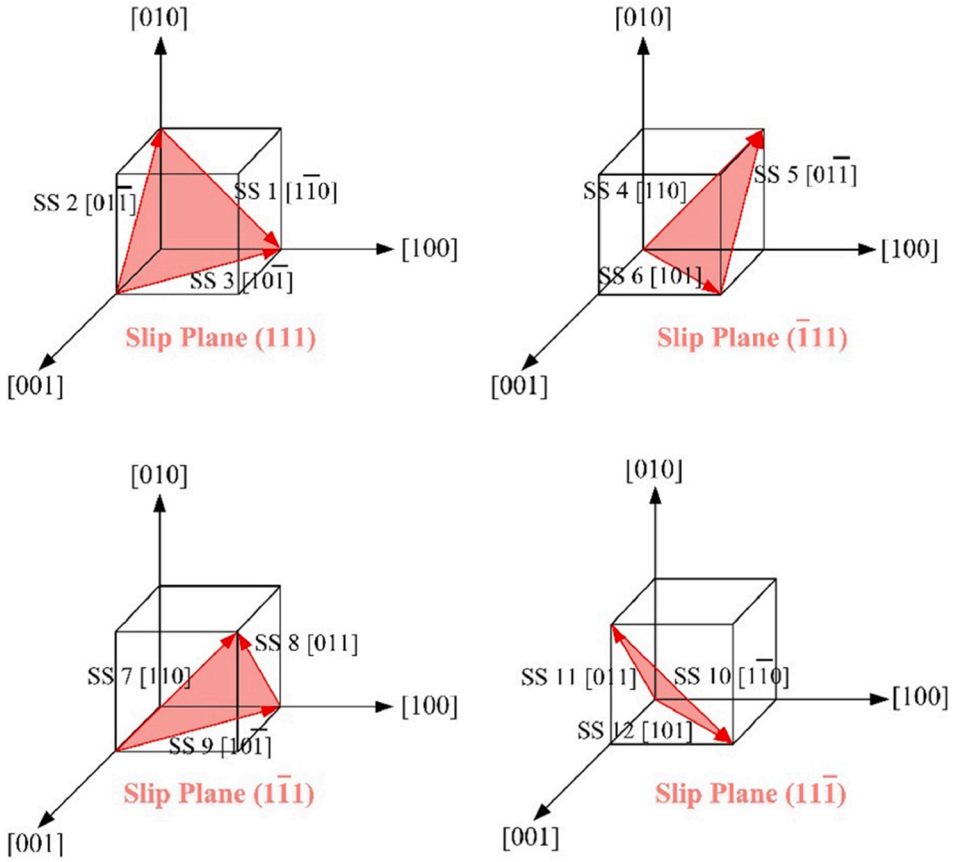

Fig. A1. FCC slip systems in reference configuration.

2.2. Microstructure reconstruction

A 3D microstructure finite element model is constructed based on the morphological and crystallographic characterisation obtained from the EBSD scan of René 88DT (Fig. 1(a)) [22]. However, this EBSD map only contains the microstructural information of the surface, hence the sub-surface microstructure is constructed based on the coherent twin boundary features in which the stacking fault plane (twin boundary) is parallel to one {1 1 1} slip plane. This {1 1 1} plane has a 60° twist along the common ⟨1 1 1⟩ with respect to the adjacent twin/parent grain. This rule is reasonably used to infer the structure of the region of interest (ROI) sub-surface (red region in Fig. 1(b)), however, the 3D nature of the neighbouring regions (blue in Fig. 1(b)) is elusive because they are general grain boundaries without regular orientation relationships. Hence, a classical extrusion assumption is used for the neighbouring blue region. Considering the previous TB inference and extrusion assumption, the model size (in the z-direction) is limited to 10 μm (1/2 average grain size) along the free surface normal. Fig. 1(c) presents two sub-views to illustrate the geometric difference between the extrusion and coherent TB inference regions, in which the normal vector in the 3D inference is parallel to the common ⟨1 1 1⟩ direction of parent/twin grain pairs.

The finite element model is developed using ~ 51,000 three-dimensional C3D8 ABAQUS elements (Fig. 2(a)) which is based on a mesh convergence study (Apendix. 4). The average element size is ~ 1.6 μm, relatively small compared to the average grain size of 20 μm. Ten elements are utilised in the thickness direction (i.e. free surface normal) in order to investigate the 3D short crack propagation behaviour sub-free surface. The applied loading boundary conditions are shown in Fig. 2(a) which aims to provide a push–pull cyclic loading as similar to the experiments, and this study focuses on the cracks initiating from the free surface. The loading history is shown in Fig. 2(b), in which the peak stress is 1140 MPa and the frequency of loading is 1 Hz (same as experiment) which is terminated when the crack grows to a length sufficient for the investigations in terms of crack propagation rates and paths, and the resulting stored energy density along a specified path-AA' in Fig. 2(a) is plotted in Fig. 2(c) to show the corresponding cyclic accumulation. The backside is set to be free because the sub-surface's microstructure is unknown, and the ramification of backside's boundary condition has been demonstrated to be weak in the stress field of free surface (Apendix. 2) after single cycle loading. The calibrated material properties used in the CP-XFEM are shown in Table 1, which are detailed in, and obtained from [22]. The critical stored energy density is chosen to be 0.1 J/m^2, which is lower than the value needed in order to give crack growth rates close to experimental measurements, but this allows more rapid crack growth, leading to fewer loading cycles needed to generate substantive crack lengths for analysis but with tractable CPU time. Differing critical stored energy densities have been considered in order to demonstrate that crack paths do not depend upon the critical stored energy chosen as shown in Apendix. 3.

In this study, a small pre-crack is inserted aligned with the TB to focus the analysis on a parallel crack near the TB. Previous experiments have demonstrated the fracture plane near a TB is aligned with one of the {1 1 1} slip planes for nickel [16]. The slip activation is calculated and shown in Fig. 3(a) to determine the slip plane trending to be fractured, in which Fig. 3(a) refers to the case of no pre-crack inserted. In Fig. 3(a), four colours are used to differentiate the regions which have differing activated slip systems. Through a crystallography analysis, this crack's fracture plane is inferred as to be parallel to the (1 1 1) slip plane in the corresponding grain, reflected by the blue colour in the same region of Fig. 3(a). Therefore, it's reasonable to insert a pre-crack at the same location with a (1 1 1)-orientation as shown in Fig. 3(b). However, there are more than one small cracks which are aligned with each other as shown in Fig. 3(c), and the order of initiation is unknown. Hence, we

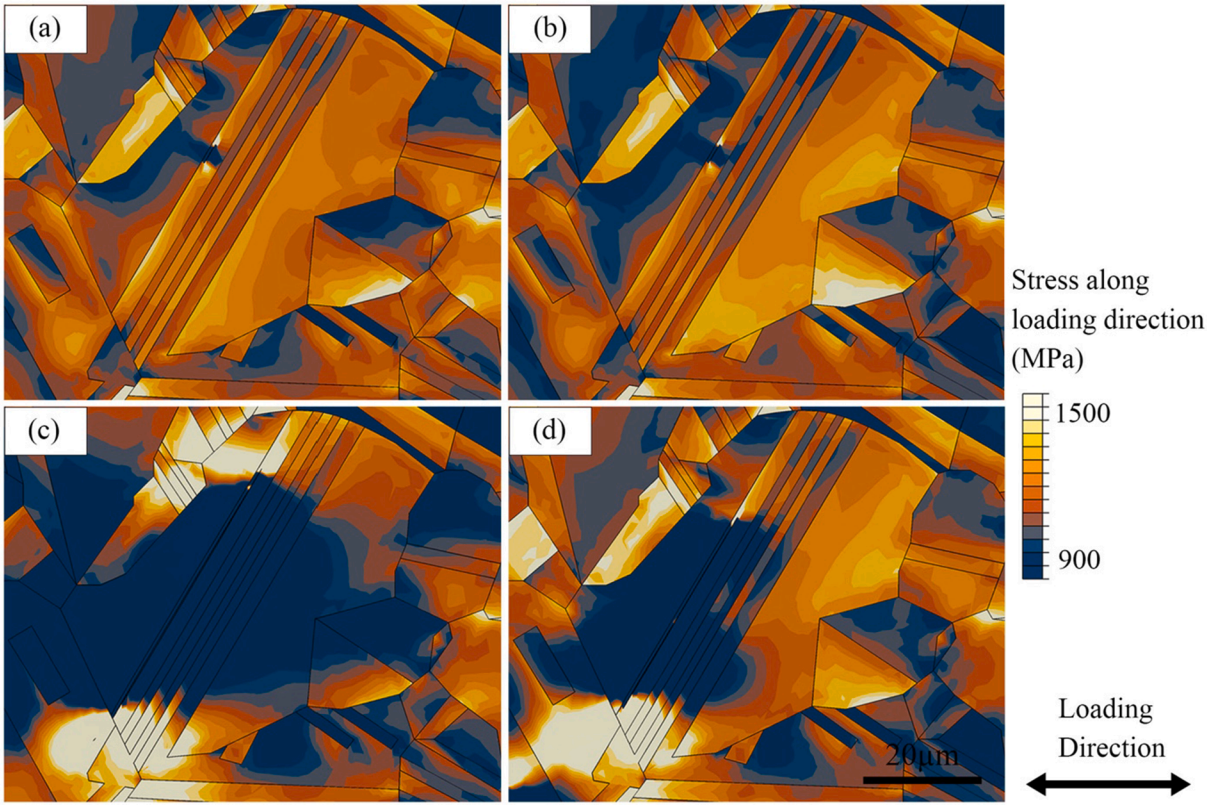

Fig. A2. The loading direction stress. (a) The displacement of back edges is fixed along free surface's normal, extracted at the peak loading of 1st cycle. (b) The displacement of backside is fixed along free surface's normal, extracted at the peak loading of 1st cycle. (c) The displacement of back edges is fixed along free surface's normal, extracted at the peak loading of 33rd cycle. (d) The displacement of backside is fixed along free surface's normal, extracted at the peak loading of 36th cycle.

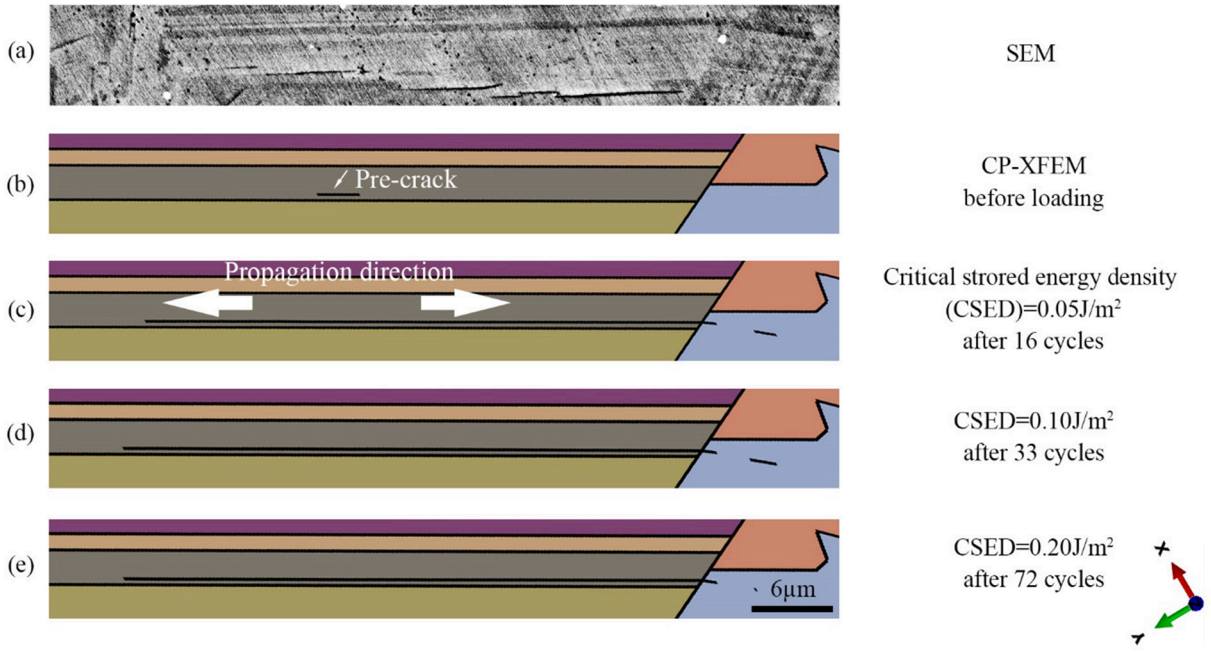

Fig. A3. (a) SEM figure captured at the end of failure time (~4200cycles); (b) Morphology obtained from CP-XFEM refers to the same region as (a), captured at the initial time step; Crack path after (c) 16 cycles with CSED = 0.05 J/m^2, (d) 33 cycles with CSED = 0.10 J/m^2 and (e) 72 cycles with CSED = 0.20 J/m^2;

arbitrarily chose one of them which is located on the mid region of TB. This pre-crack is inserted across two elements on the free surface and it has an absolute length of 3.15 μm (on the global XY plane). The length of pre-crack is chosen to be that of two elements in size which is appropriate for driving the propagation within limited cycles and facilitates enough regions where is can be investigated. The 2D crack path

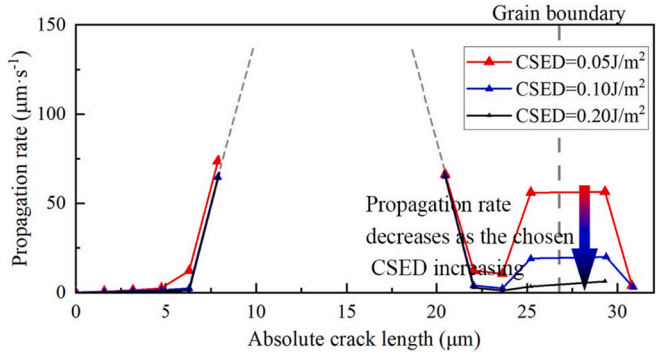

Fig. A4. Crack propagation rate calculated from the paths on free surface in differing CSED magnitudes. Propagation rate decreases (more cycles needed for driving crack growth) as the chosen CSED increasing.

(projected 3D fracture plane on free surface) is plotted by a black dashed line in Fig. 3(b) which agrees with the SEM observation in Fig. 3(c), demonstrating the validity of this pre-crack. That is, the intersection line (black dashed line in Fig. 3(b)) between slip plane and free surface is aligned with the cracks circled in Fig. 3(c).

3. Results & discussion

3.1. Fatigue crack path and propagation rate on the free surface

Crack growth paths and rates are firstly considered in the microstructure shown in Fig. 3 by focusing on the twinned region of the model microstructure shown in Fig. 4 (a), into which a short crack has been introduced prior to applying fatigue loading cycles. Comparisons of CP-XFEM calculations with experimental observations are presented and discussed. Three cracks can be seen in the SEM figure, which are all parallel to the adjacent TB [22]. These cracks were found to nucleate and grow along (1 1 1) slip planes in the experiment and are shown after sample fatigue failure. In the model, only a single short crack is introduced, and Fig. 4(b) and (c) show the initial state and its predicted evolution from the CP-XFEM respectively, in which the inserted pre-crack (Fig. 4(b)) propagates along the TB until it touches the grain boundary at the tip of the TB in Fig. 4(c). A deflection of crack path can then be observed after the crack-tip traverses the grain boundary due to the inhomogeneity of the elastic stored energy field, which will be discussed around Fig. 5. In addition, this deflection of crack path also may be influenced by the chosen critical elastic stored energy density as shown in Fig. A.3(a). In the initiating grain, the crack plane is identified to be (1 1 1) which is parallel to the twin boundary if the fracture plane is assumed to be aligned with one of the slip planes [16], thereby in agreement with the SEM observation [22]. The experimental observation of multiple parallel cracks may arise simply because the separated cracks grow on parallel planes which are very close to each other, and may not in fact be strongly influenced by the TB. Previous work [22] shows that the local anisotropy and constraint at TBs leads to the onset of slip on planes which are parallel to the TB (as well as inclined) thus potentially favouring further the development of cracking as observed.

Elastic stored energy density is employed in this study which controls the calculated rate of short crack propagation. While the critical stored energy density has been selected to give significant crack lengths within a relatively small number of loading cycles, it is nonetheless informative to study the relative change of the propagation rate as the predicted crack grows through the microstructure. The elastic stored energy density contours are provided in Fig. 5(a) and (b), captured after 20 cycles (unloaded state) and 29.75 cycles (reversed peak loading) respectively. The propagation rate on the free surface is calculated and plotted against the absolute crack length as shown in Fig. 5(c). Here the absolute crack length is defined by the projected length of the 3D fracture plane on the free surface. In Fig. 5(c), a low but increasing crack growth rate is predicted initially up to crack length of ~ 7 μm. At this stage, Fig. 5(b) shows that the crack tip is about to grow into a region of very high stored energy density (which in fact is in excess of the critical stored energy density), and as it does so, Fig. 5(c) shows a rapid increase in growth rate, and the crack grows to a length of 20 μm very rapidly indeed, and within a single loading cycle such that its rate is undefined (and shown by the broken lines/gap in Fig. 5(c)). Current results are obtained using 80 time increments per cycle, but up to 320 time increments per cycle have been tested for the convergence. All these increments show the same region with very rapidly propagation rate and high stored energy density. The region with high stored energy density is developed by the combination of parallel slip and strong elastic anisotropy, as demonstrated in [22], and is established very early in the fatigue loading, well before the crack propagation develops. That is, a crack would have probably initiated within this area before the

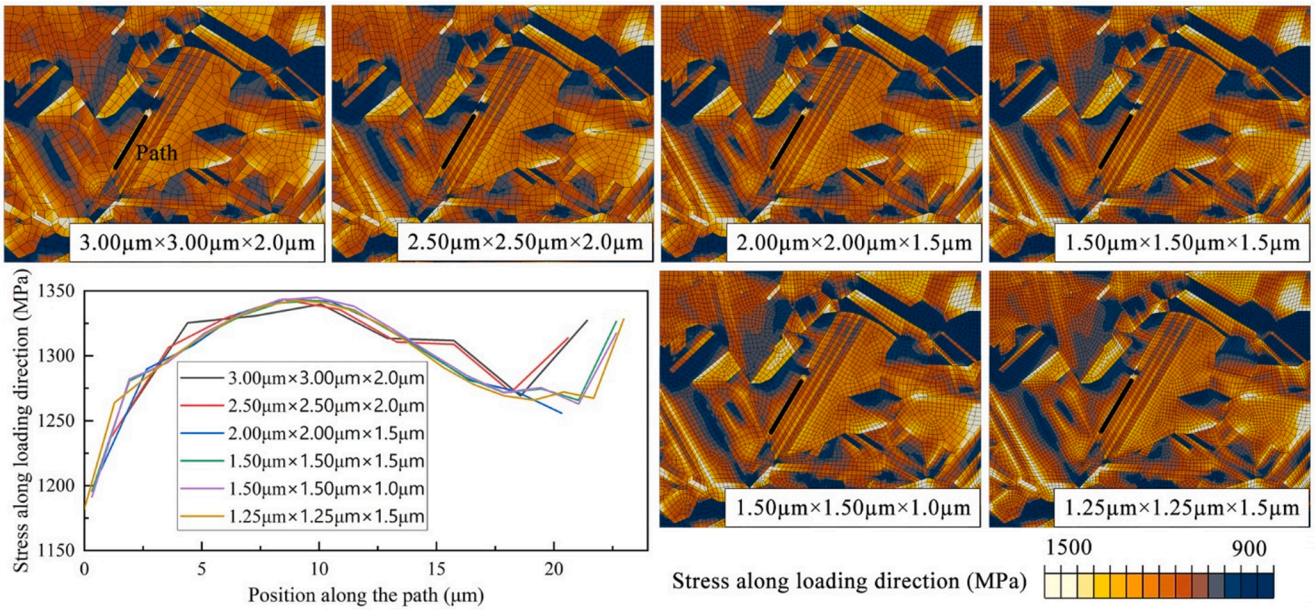

Fig. A5. Mesh convergence studies using six differing mesh sizes.

simulated crack would reach it. However, detailed experimental data to define the precise location of crack nucleation was not available such that the modelled initial crack was located simply to reflect the generic experimental observation. From a length of ~ 20 μm, however, the rate retards as a consequence of the crack tip having grown out of and beyond the region of very high, pre-existing, stored energy density. Further retardation and then some acceleration in growth occur because of the crack tip field beginning to interact with the grain boundary ahead, reflecting again the microstructural sensitivity and the heterogeneous field of stored energy density (the driving force used in this study), and the importance of grain boundary constraint and elastic anisotropy. In addition, the retardation around the end of the TB is also associated with the CSED chosen as shown in Apendix 3. An important observation is that the crack growth rate as it develops along the twin boundary is predicted to be very high compared with subsequent growth such that it could be considered effectively to be part of the instantaneous crack nucleation process, since previous work [22] demonstrated the nucleation of cracks at the TBs. Subsequent crack propagation is shown and anticipated to be much slower (by at least an order of magnitude). It is noted that the study so far has been confined to the free surface analysis only, whereas the crack is in fact modelled in 3D along with the twin morphology and crystallography. Hence the sub-surface behaviour is considered in the next section.

3.2. 3D crack propagation sub-surface

In 3D, the crack-front may in fact take a tortuous path as it cuts through the volume below the free surface. The crack-front may develop in a complicated manner with load cycling giving rise to non-planar cracks with a non-smooth front, with much more complexity than can be captured in 2D, hence understanding the mechanisms of 3D crack propagation is important. In this section, the 3D propagation rate is calculated in two different ways, and the evolution of these rates with respect to the microstructure ahead of crack-front are analysed.

The fracture plane developing in the current study is in fact found to be a near-smooth plane without sharp facets (there exists a ~ 8.89° deviation at the grain boundary, marked in Fig. 6(b)), such that the 3D fracture plane can be decomposed into a series of adjacent discrete 2D cracks which are similar to the paths observed on the free surface. Most of the series of discretised 2D cracks were found to grow from the free surface and towards the sub-surface. Fig. 6(a) shows the 3D crack propagation rate versus the crack front length along the defined propagation direction (Fig. 6(b)). The right-axis in Fig. 6(a) is the distance away from the pre-crack on the free surface. Most of the propagation rates shown in Fig. 6(a) are positive which means these crack paths grow towards the sub-surface. A few points located around the grain boundary (the end of TB, marked in Fig. 6(b)) show negative values, which means the propagation direction is towards the free surface. Some clear peaks can be observed around the end of the TB, corresponding to the region within which the stored energy density is high giving rise to correspondingly high growth rates, as discussed in Section 3.1. Fig. 5 and the peaks of Fig. 6 together show the crack propagation rate is high when the fracture plane is parallel to the TB. In addition, the fairly uniform decrease in propagation rate occurring (in the region of ~ 20 μm on the right axis in Fig. 6(a)) following these high rates shows a resistance to crack growth exists and is generated by the grain boundary (the end of TB, marked in Fig. 6(b)).

An alternative approach to quantifying the propagation rate in 3D is shown in Fig. 7, in which the classical 2D crack length is replaced by the area of the fracture plane. This fracture plane is the same one in Fig. 6 (b), and both are captured after 32.5 cycles. The perimeter of the fracture plane is extracted in equal cycles as shown in Fig. 7(a). In this approach, the propagation direction is always changing because the next fractured area/element is discretely located along the perimeter of fracture plane, which generates multiple directions as the grey arrows shown in Fig. 7(a). In Fig. 7(b), a region of high area crack growth rate (marked by a grey arrow) can be seen near the left side of the grain boundary. This high growth rate occurs at the location near to the region of high stored energy density in Fig. 5(c) and the corresponding peaks in growth rate in Fig. 6(a) as anticipated, with the highest crack growth rates occurring along a path in direction $\boldsymbol{l}_{\text{main prop.}}$ which is roughly plotted. The evolution of area propagation rate is quantitively shown in Fig. 7(b) where the location of the grain boundary (the end of TB) is marked by the grey dashed line, linking with Fig. 7(a), and consistent with the location of the end of the TB mentioned above. In Fig. 7(b), the horizontal position of the grain boundary (the end of the TB) is determined by the time when the fracture plane firstly touches the grain boundary. A lower rate can be observed ahead (on the left side) of the grain boundary. The trend of this evolution is basically reflecting the observations in Fig. 5(c), showing that the effect of the grain boundary at the end of the TB is to resist crack growth, reducing crack propagation rate. However, a higher area propagation rate can be observed when the crack front locates just prior to the grain boundary. The higher area rate observed simply reflects that the quantity reported (rate of area change) does not contain information on directionality. That is, crack growth measured on the free surface (2D) near the TB is very different to sub-surface growth (3D), as shown in Fig. 7(a). Hence, the higher area propagation rate reflects the dominance of sub-surface crack branches (small grey arrows $\boldsymbol{l}_{\text{sub prop.}}$ in Fig. 7(a)) as opposed to free-surface growth shown by the red narrow $\boldsymbol{l}_{\text{fs prop}}$ shown in Fig. 7(a), which is exactly the 2D propagation rate on the free surface reflected in Fig. 5(c). That is, these sub-branches (refers to all prop. directions excluding the $\boldsymbol{l}_{\text{fs prop}}$) generate the rate acceleration ahead of grain boundary which is different from the 2D result in Fig. 5(c). In addition, the region of high stored energy in Fig. 5(c) is reflected in this approach in which a clear peak is observed at ~ 90 μm^2 corresponding to the region in Fig. 5(c).

3.3. Elastic anisotropy, slip activation and crack propagation path

Nickel alloy intrinsically has a high elastic anisotropy, which results in stress concentration near grain boundaries [9]. Previous work has demonstrated that strain localization can be developed near TBs due to the high elastic anisotropy, leading to high GND density and elastic stored energy density, further facilitating fatigue crack nucleation [22]. However, as the crack grows, it of course interacts with a changing microstructure, resulting in the establishment of differing and changing local stress fields and hence slip activations. It's useful to investigate the effect of elastic anisotropy in short crack propagation because it can be representative of the differing microstructures encountered by growing short cracks. In this work, the natural high elastic anisotropy (Zener ratio = 2.44, which is determined by $2C_{44}/(C_{11}\text{-}C_{12})$, C_{11}, C_{12} and C_{44} are the three independent elastic constants in FCC crystal) gives rise to predicted crack growth which is parallel to the TB as shown in Fig. 8(a) for cycle 30, where the fracture plane is within the (1 1 1) slip plane.

To investigate the effect of elastic anisotropy, the elastic properties of the grains local to the crack (all grains shown in Fig. 8(b)) are modified to be elastically isotropic where the Young's modulus along all directions is equal to 216.9GPa which is averaged from the anisotropic E ⟨1 1 1⟩ and E ⟨1 0 0⟩ values (Fig. 8(a)). In Fig. 8(b), the predicted crack can be seen to be inclined to the TB, and the main fracture plane is identified as $(\bar{1}11)$. In addition, the rate of crack propagation along the twin plane is lower than that for anisotropic elasticity in Fig. 8(a) before entering the very high rate region in Fig. 5(c). This lower rate results from the activation of a slip system inclined to the TB, and it develops associated with the loss of elastic anisotropy. The propensity for slip (as determined from the CP model) in the grains of interest is shown in Fig. 9 (a) and (b), in which parallel slip (blue in Fig. 9(a)) and inclined slip (green in Fig. 9(b)) in the grain adjacent to the twin within which the crack grows, are predicted after just 1.25 cycles. The corresponding stress fields in Fig. 9(c) and (d) show that higher stress concentration develops in the elastically anisotropy crystal in Fig. 9(c) as opposed to

the elastically isotropic case in Fig. 9(d). In addition, the resolved shear stresses have been extracted and those for slip systems containing the maximum values are shown in Fig. 9(e) and (f) for elastic anisotropy and isotropy respectively. The maximum resolved shear stress (RSS) reflects the crystal orientation. In Fig. 9(e) high RSS can be observed near the TB when the elasticity is anisotropic, and this high RSS is identified to be on the parallel slip system through Fig. 9(a). In Fig. 9(f), the RSS field shows a relatively homogeneous distribution and low magnitude near the TB, which corresponds to the inclined slip system (green colour in Fig. 9(b)).

3.4. Crystallography associated with twist angle

A coherent twin boundary has a crystallographic orientation in which parent grain and twin grain have two aligned {1 1 1} slip planes, and there is a 60° twist between these two planes, where the twist axis is their common ⟨1 1 1⟩. Based on this special microstructure, a local stress field may exist, resulting in parallel cracking along the TB. To examine the potential effect of the twist angle, the twist in one grain of the twin/parent pair is varied. However, before this study is carried out, the relevant parts of the microstructure are simplified in order to remove the lamellar structure, which is shown in Fig. 10(a). This modification results in consideration of two differently orientated grains (with a twist angle between them) representing the twin-parent pair, such that the mechanistic link between the crystallography (twist angle) and crack growth behaviour may be analysed without the complication of the lamellar structure. In the modified microstructure, Grain A (pink) is maintained as before, and only Grain B (green) is progressively twisted about their common ⟨1 1 1⟩ by 0° to120° as shown in Fig. 10(b). All analyses are conducted with the original, full elastic anisotropy, with Zener ratio of 2.44.

The evolution/heterogeneity of stress fields versus twist angles can be seen in Fig. 11, in which twist 0° and 120° are identical due to the 120° periodic symmetry along ⟨1 1 1⟩ in FCC. Twist 0°/120° has the same twist angle as the actual TB case, and stress concentrations can still be clearly seen in twist 0°/120° like Fig. 9(c). This stress concentration is mitigated as the twist angle is increased to 60°. Here, crystallography analysis identified the case of twist 60° is a single crystal configuration in which the parent grain's crystal orientation is effectively identical to the twin grain's crystal orientation. Homogeneous stress field (twist 60° from actual configuration) reflects this identical crystal orientation, which remove the stress concentration as observed in twist 0°/120° (actual TB configuration). This homogeneous stress field (twist 60° from actual configuration, corresponding to a local single crystal) returns to being heterogeneous (twist 120°) but with a differing route with respect to twist 0° to 60°. Hence, this evolution demonstrates the stress concentration is associated with the twist angle. When the twist angle approaches to 0°/120° (corresponding to the actual configuration of the TB which a 60° twist along ⟨1 1 1⟩), the more concentrated stress field the near TB is apparent at a very early stage in the deformation.

The morphology of the resulting predicted crack paths corresponding to the differing twist angles are shown in Fig. 12, which are the results given by running many fatigue cycles sufficient to propagate the initial crack. Because the twist between TB/parent grains lead to differing favoured slip system activations, differing numbers of cycles are required to lead to the crack growth shown for each case. In Fig. 12, as before for reasons of symmetry, twist angles of 0° and 120° show identical crack shape. The primary path of the crack deviates from parallel to the TB as the twist angle increasing from 0° to 60°. This interesting evolution reflects the key role of the stress concertation near the TB. Moreover, the key microstructure feature (twist angle) is demonstrated to be one strong factor which affects the crack propagation behaviour near the TB.

4. Conclusions

A 3D CP-XFEM model is reconstructed from a polycrystal nickel alloy fatigue experiment to investigate the mechanistic understanding of short crack propagation near a twin boundary. The effects of elastic anisotropy and the twist crystallography associated with the coherent twin boundary are assessed based on a specified microstructure of René 88DT which contains a large fraction of annealing twins, and key conclusions are:

1. Short crack growth parallel to the coherent twin boundary is predicted, which shows good agreement with experimental observation. A very high propagation rate (at least an order of magnitude) occurs as the fracture plane develops along the twin boundary, such that it may effectively be deemed to be as aspect of the crack nucleation process, in which the crack would have probably initiated within this area before the simulated crack would reach it.
2. The strong elastic anisotropy is demonstrated to be a key contributor to the TB stress concentration and explains why TB cracks are planar and parallel to the twin (1 1 1) plane. Simulated elastic isotropy shows that non-planar cracks develop with different growth rates, and that they are in planes inclined, and not parallel to the TB.
3. Short fatigue crack morphology is sensitive to the twist angle along the common ⟨1 1 1⟩ of the twin/parent pair. This twist angle affects TB stress concentration and hence crack morphology. The 60° twist angle (refers to the actual TB configuration, and the twist 0° /120° in Fig. 11 and Fig. 12) gives rise to the highest local TB stresses and explains preferential crack nucleation and rapid crack growth rate parallel to the TB.

Declaration of Competing Interest

The authors declare that they have no known competing financial interests or personal relationships that could have appeared to influence the work reported in this paper.

Data availability

Data will be made available on request.

Acknowledgement

Xiaoxian Zhang would like to thank the funding provided by China Scholarship Council and Imperial College London. Fionn P.E. Dunne acknowledges with gratitude his Royal Academy of Engineering / Rolls-Royce research chair funding.

Appendix 1

Fig. A.1.

Appendix 2

The backside is set to be free because the sub-surface's microstructure is unknown. However, it's well-known that the free surface's behaviour may be affected by the backside's constraint if the grain layers along extrusion direction is less. Hence, a study is conducted to examine the ramification of the backside's boundary condition using two extreme loading boundary conditions as below. Fig. A.2(a) and (c) show the loading boundary condition used in the main text in which only the two back edges are fixed, Fig. A.2(b) and (d) show a loading boundary condition in which the whole back side is fixed. These stress contours are extracted at the peak loading of 1st cycle and the end step of crack propagation, in which the loading direction stress field is similar on free surface at the peak loading of 1st cycle as shown in Fig. A.2 (a) and (b). And this similarity decreases after multiple cycles as shown in Fig. A.2 (c) and (d). However, the differences in terms of crack morphology and crack propagation are still weak in which the crack propagates along the twin boundary with a high speed. Hence, it's reasonable to argue this loading boundary condition can be used in this

study to investigate the effect of twined microstructure in short crack propagation and will not strongly affect the scientific conclusions associated with the strain/slip localization and stress concentration around the coherent twin boundary.

Appendix 3

Critical stored energy density (CSED) is employed as the criterion of propagating crack. Basically, higher CSED refers to more cycles to failure. CSED is one property of materials which can be calculated from experimental measurement, however, a low CSED is chosen in this study to obtain a propagated crack with less simulated cycles, which can effectively save the computational time and disk space. However, potential ramification caused by differing CSEDs can't be ignored due to the non-linear plasticity nature. Therefore, an examination for differing CSED's effect is conducted and the result is shown in Fig. A3 and Fig. A.4 in terms of crack path and propagation rate respectively on free surface. Fig. A.3 provided a comparison between SEM (Fig. A.3(a)) and CP-XFEM in same region but with differing CSEDs. Fig. A.3(b) shows the initial morphology before cyclic loading. Fig. A.3 (c)(d) and (e) show highly similar crack paths, and all these paths agree with the SEM observation which presents a parallel crack with respect to the adjacent TB. In addition, a slight prohibition can be observed after the end of TB in Fig. A.3 (e) which may be caused by the higher CSED.

Crack propagation is assumed to be driven by the elastic stored energy density, and the propagation rate of crack path on surface is calculated versus the absolute crack length, as shown in Fig. A.4. It can be clearly seen that three CSEDs show similar increasing-trends as crack growing along the TB, and then decrease near grain boundary (the end of TB). At most of measured positions (excluding the dashed gap), higher CSED shows lower propagation rate (more cycles needed for driving crack growth) which agrees the expectation. For the gap around 15 μm as discussed before, all CSEDs present a very high and same propagation rate, this is because one concentred stored energy field (dashed mark in previous Fig. 5(b)) exists ahead of the initial crack-tip by ~ 9 μm but develops early. The stored energy density within this region exceeds the corresponding CSED, hence one element is bisected when one time increment is completed. Therefore, the calculated propagation rate within this region is limited by the time increment (in this study, using ~ 80 increments for each cycle), the actual propagation rate is expected to be higher than the Fig. A-4 shown. Nevertheless, differing CSEDs show a good convergence in terms of crack path and crack propagation rate. Therefore, it's reasonably to use 0.10 J/m^2 as the CSED to save the computational time and disk space in previous sections to discuss the effect of crystallography and elastic anisotropy to the short crack propagation near the coherent twin boundary.

Appendix 4

A mesh convergence study is shown to ensure the element size is sufficient for the CP-XFEM models to obtain reliable micromechanical results. The study employs same microstructural morphologies with six differing mesh refinements (specified in terms of numbers of elements, namely 9305 (element size 3.0 μm × 3.0 μm × 2.0 μm), 12,045 (2.5 μm × 2.5 μm × 2.0 μm), 21,889 (2.0 μm × 2.0 μm × 1.5 μm), 35,546 (1.5 μm × 1.5 μm × 1.5 μm), 51,030 (1.5 μm × 1.5 μm × 1.0 μm) and 51,449 (1.25 μm × 1.25 μm × 1.5 μm). The stress field ahead of crack-tip and along the path for the six meshing schemes are shown in Fig A.5. It can be seen that coarse meshes (3.0 μm × 3.0 μm × 2.0 μm, 2.5 μm × 2.5 μm × 2.0 μm, black and red lines in the line figure) haven't shown the convergent evolution but the remaining finer meshes (blue, green, violet and brown) convergence. As a consequence, the mesh scheme (1.5 μm × 1.5 μm × 2.0 μm with 51,030 elements totally) is selected for this study based on the considerations of computational time, disk space.

References

[1] Suresh S. Fatigue of materials. Cambridge University Press; 1998.
[2] Jiang R, Song YD, Reed PA. Fatigue crack growth mechanisms in powder metallurgy Ni-based superalloys—A review. Int J Fatigue 2020;141(May):105887. https://doi.org/10.1016/j.ijfatigue.2020.105887.
[3] Socha G. Experimental investigations of fatigue cracks nucleation, growth and coalescence in structural steel. Int J Fatigue 2003;25(2):139–47. https://doi.org/10.1016/S0142-1123(02)00068-3.
[4] Reed RC. The superalloys: fundamentals and applications. Cambridge University Press; 2008.
[5] Peng Z, Zou J, Wang X. Microstructural characterization of dislocation movement during creep in powder metallurgy FGH96 superalloy. Mater Today Commun 2020;25(June):101361. https://doi.org/10.1016/j.mtcomm.2020.101361.
[6] Miao J, Pollock TM, Wayne Jones J. Crystallographic fatigue crack initiation in nickel-based superalloy René 88DT at elevated temperature. Acta Mater 2009;57(20):5964–74. https://doi.org/10.1016/j.actamat.2009.08.022.
[7] Yeratapally SR, Glavicic MG, Hardy M, Sangid MD. Microstructure based fatigue life prediction framework for polycrystalline nickel-base superalloys with emphasis on the role played by twin boundaries in crack initiation. Acta Mater 2016;107:152–67. https://doi.org/10.1016/j.actamat.2016.01.038.
[8] Stinville JC, Lenthe WC, Echlin MP, Callahan PG, Texier D, Pollock TM. Microstructural statistics for fatigue crack initiation in polycrystalline nickel-base superalloys. Int J Fract 2017;208(1–2):221–40. https://doi.org/10.1007/s10704-017-0241-z.
[9] Heinz A, Neumann P. Crack initiation during high cycle fatigue of an austenitic steel. Acta Metall Mater 1990;38(10):1933–40. https://doi.org/10.1016/0956-7151(90)90305-Z.
[10] Stinville JC, Lenthe WC, Miao J, Pollock TM. A combined grain scale elastic-plastic criterion for identification of fatigue crack initiation sites in a twin containing polycrystalline nickel-base superalloy. Acta Mater 2016;103:461–73. https://doi.org/10.1016/j.actamat.2015.09.050.
[11] Stinville JC, Callahan PG, Charpagne MA, Echlin MP, Valle V, Pollock TM. Direct measurements of slip irreversibility in a nickel-based superalloy using high resolution digital image correlation. Acta Mater 2020;186:172–89. https://doi.org/10.1016/j.actamat.2019.12.009.
[12] Gustafson S, Ludwig W, Shade P, Naragani D, Pagan D, Cook P, et al. Quantifying microscale drivers for fatigue failure via coupled synchrotron X-ray characterization and simulations. Nat Commun 2020;11(1):1–10. https://doi.org/10.1038/s41467-020-16894-2.
[13] Sangid MD, Maier HJ, Sehitoglu H. The role of grain boundaries on fatigue crack initiation - An energy approach. Int J Plast 2011;27(5):801–21. https://doi.org/10.1016/j.ijplas.2010.09.009.
[14] Sangid MD, Maier HJ, Sehitoglu H. An energy-based microstructure model to account for fatigue scatter in polycrystals. J Mech Phys Solids 2011;59(3):595–609. https://doi.org/10.1016/j.jmps.2010.12.014.
[15] Miao J, Pollock TM, Wayne Jones J. Microstructural extremes and the transition from fatigue crack initiation to small crack growth in a polycrystalline nickel-base superalloy. Acta Mater 2012;60(6–7):2840–54. https://doi.org/10.1016/j.actamat.2012.01.049.
[16] Liu L, Husseini NS, Torbet CJ, Lee WK, Clarke R, Jones JW, et al. In situ synchrotron X-ray imaging of high-cycle fatigue crack propagation in single-crystal nickel-base alloys. Acta Mater 2011;59(13):5103–15. https://doi.org/10.1016/j.actamat.2011.04.042.
[17] Stinville JC, Vanderesse N, Bridier F, Bocher P, Pollock TM. High resolution mapping of strain localization near twin boundaries in a nickel-based superalloy. Acta Mater 2015;98:29–42. https://doi.org/10.1016/j.actamat.2015.07.016.
[18] Kobayashi S, Hirata M, Tsurekawa S, Watanabe T. Grain boundary engineering for control of fatigue crack propagation in austenitic stainless steel. Procedia Eng 2011;10:112–7. https://doi.org/10.1016/j.proeng.2011.04.021.
[19] Abuzaid W, Oral A, Sehitoglu H, Lambros J, Maier HJ. Fatigue crack initiation in Hastelloy X - The role of boundaries. Fatigue Fract Eng Mater Struct 2013;36(8):809–26. https://doi.org/10.1111/ffe.12048.
[20] Ravi P, Naragani D, Kenesei P, Park JS, Sangid MD. Direct observations and characterization of crack closure during microstructurally small fatigue crack growth via in-situ high-energy X-ray characterization. Acta Mater 2021;205:116564. https://doi.org/10.1016/j.actamat.2020.116564.
[21] Zhang X, Dunne FPE. 3D CP-XFEM modelling of short crack propagation interacting with twist/tilt nickel grain boundaries. J Mech Phys Solids 2022. https://doi.org/10.1016/j.jmps.2022.105028.
[22] Zhang X, Stinville JC, Pollock TM, Dunne FPE. Crystallography and elastic anisotropy in fatigue crack nucleation at nickel alloy twin boundaries. J Mech Phys Solids 2021;155(March):104538. https://doi.org/10.1016/j.jmps.2021.104538.
[23] Li LL, Zhang ZJ, Zhang P, Wang ZG, Zhang ZF. Controllable fatigue cracking mechanisms of copper bicrystals with a coherent twin boundary. Nat Commun 2014;5. https://doi.org/10.1038/ncomms4536.
[24] Li L, Zhang Z, Zhang P, Zhang Z. Progress in Materials Science A review on the fatigue cracking of twin boundaries : Crystallographic orientation and stacking fault energy. Prog Mater Sci 2023;131(August 2022):101011. https://doi.org/10.1016/j.pmatsci.2022.101011.
[25] Latypov MI, Stinville JC, Mayeur JR, Hestroffer JM, Pollock TM, Beyerlein IJ. Insight into microstructure-sensitive elastic strain concentrations from integrated computational modeling and digital image correlation. Scr Mater 2021;192:78–82. https://doi.org/10.1016/j.scriptamat.2020.10.001.

[26] Wan VVC, Maclachlan DW, Dunne FPE. A stored energy criterion for fatigue crack nucleation in polycrystals. Int J Fatigue 2014;68:90–102. https://doi.org/10.1016/j.ijfatigue.2014.06.001.
[27] Zheng Z, Prastiti NG, Balint DS, Dunne FPE. The dislocation configurational energy density in discrete dislocation plasticity. J Mech Phys Solids 2019;129:39–60. https://doi.org/10.1016/j.jmps.2019.04.015.
[28] Chen B, Jiang J, Dunne FPE. Is stored energy density the primary meso-scale mechanistic driver for fatigue crack nucleation? Int J Plast 2018;101(December 2017):213–29. https://doi.org/10.1016/j.ijplas.2017.11.005.
[29] Wilson D, Wan W, Dunne FPE. Microstructurally-sensitive fatigue crack growth in HCP, BCC and FCC polycrystals. J Mech Phys Solids 2019;126:204–25. https://doi.org/10.1016/j.jmps.2019.02.012.
[30] Song K, Wang K, Zhang L, Zhao L, Xu L, Han Y, et al. Insights on low cycle fatigue crack formation and propagation mechanism: A microstructurally-sensitive modeling. Int J Plast 2022;154(March):103295. https://doi.org/10.1016/j.ijplas.2022.103295.
[31] Asaro RJ, Rice JR. Strain localization in ductile single crystals. J Mech Phys Solids 1977;25(5):309–38. https://doi.org/10.1016/0022-5096(77)90001-1.
[32] Dunne FPE, Rugg D, Walker A. Lengthscale-dependent, elastically anisotropic, physically-based hcp crystal plasticity: Application to cold-dwell fatigue in Ti alloys. Int J Plast 2007;23(6):1061–83. https://doi.org/10.1016/j.ijplas.2006.10.013.
[33] Dunne FPE, Kiwanuka R, Wilkinson AJ. Crystal plasticity analysis of micro-deformation, lattice rotation and geometrically necessary dislocation density. Proceedings of the Royal Society A: Mathematical, Physical and Engineering Sciences 2012;468(2145):2509–31. https://doi.org/10.1098/rspa.2012.0050.
[34] Cheng J, Ghosh S. A crystal plasticity FE model for deformation with twin nucleation in magnesium alloys. Int J Plast 2015;67:148–70. https://doi.org/10.1016/j.ijplas.2014.10.005.
[35] Dai H. Geometrically-necessary dislocation density in continuum plasticity theory, FEM implementation and applications. Massachusetts Institute of Technology); 1997. Doctoral dissertation,.
[36] Arsenlis A, Parks DM. Crystallographic aspects of geometrically-necessary and statistically-stored dislocation density. Acta Mater 1999;47(5):1597–611. https://doi.org/10.1016/S1359-6454(99)00020-8.
[37] Dunne, & Petrinic, N. (2005). Introduction to computational plasticity. Oxford University Press.
[38] Nguyen GD, Korsunsky AM, Belnoue JPH. A nonlocal coupled damage-plasticity model for the analysis of ductile failure. Int J Plast 2015;64:56–75. https://doi.org/10.1016/j.ijplas.2014.08.001.
[39] Wilson D, Dunne FPE. A mechanistic modelling methodology for microstructure-sensitive fatigue crack growth. J Mech Phys Solids 2019;124:827–48. https://doi.org/10.1016/j.jmps.2018.11.023.
[40] Wilson D, Zheng Z, Dunne FPE. A microstructure-sensitive driving force for crack growth. J Mech Phys Solids 2018;121:147–74. https://doi.org/10.1016/j.jmps.2018.07.005.
[41] Karamitros V, MacLachlan DW, Dunne FPE. Mechanistic fatigue in Ni-based superalloy single crystals: A study of crack paths and growth rates. J Mech Phys Solids 2022;158(June 2021):104663. https://doi.org/10.1016/j.jmps.2021.104663.